ACS Biomaterials SCIENCE & ENGINEERING

pubs.acs.org/journal/abseba

Article

Multi-organ-on-a-Chip: The Gut and Inflammatory Diseases

Dimple Sajin, Shehzahdi S. Moonshi, Haotian Cha, Fahima Akther, Jun Zhang, Nam-Trung Nguyen, and Hang Thu Ta*

Cite This: https://doi.org/10.1021/acsbiomaterials.5c00208

Read Online

ACCESS | Metrics & More | Article Recommendations | Supporting Information

ABSTRACT: Alteration of the human gut is frequently linked to various diseases. While animal models are valuable tools for studying the interactions between hosts and microbes, there is still a need for a physiologically relevant *in vitro* gut model. This study presents the development of an integrated microfluidic platform that simultaneously incorporates features of both the gut and vascular systems. The gut chamber incorporates cellular layers resembling epithelial cells, while the vascular channel mimics blood vessel endothelial cells and incorporates shear stress forces relevant to blood flow. This multiorgan model provides a more accurate, *in vitro* representation of human physiological processes and offers new opportunities for studying gut−heart interactions and the impact of inflammatory diseases. The platform's versatility and scalability make it a promising tool for high-throughput screening, disease modeling, and precision medicine applications.

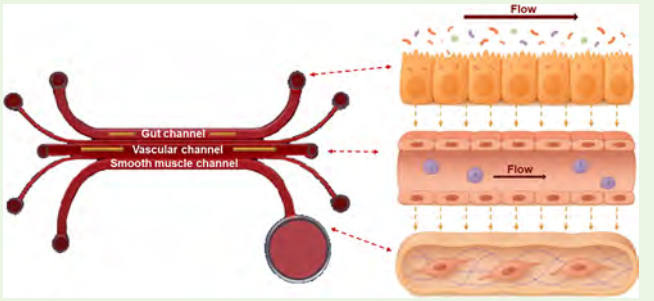

KEYWORDS: *multiorgan, microfluidics, human gut, IBD, cardiovascular disease, blood vessel*

1. INTRODUCTION

It is well known that the human intestine plays a crucial role in digestion, absorption, and secretion, while also creating a protective epithelial barrier that separates the digestive environment from the body.[1] Numerous and diverse microbial species inhabit the lower gastrointestinal tract. An imbalance in the composition and function of these intestinal microbes is often termed gut microbiota disorder. This disorder is linked to various diseases, such as inflammatory bowel disease (IBD), diabetes, obesity, cancer, and, more recently, neurodegenerative and cardiovascular diseases (CVD).[2−5] Nevertheless, a comprehensive grasp of the essential molecular mechanisms that govern host−microbe interactions and their potential influence on immune regulation, drug metabolism, nutrition, and infection remain largely elusive.[6−8] Thus, the human microbiome is increasingly recognized as a crucial factor affecting human health, highlighting the importance of studying the interaction between the host and microbiome in the context of drug development, disease progression, and treatment.

To investigate the relationship between the gut microbiome and host cells in a more efficient, rapid, and cost-effective manner, significant efforts have been made to create experimental *in vitro* and *ex vivo* models of the human intestine. These models enable the analysis of intestinal pathophysiology under various conditions, including the presence or absence of a living microbiome.[9−11] So far, the most frequently employed *in vitro* intestinal model is the utilization of human intestinal epithelial cells (e.g., Caco-2 and/or HT-29 cells) that are coated with an extracellular matrix (ECM) and seeded on a porous membrane within Transwell insert culture devices.[12−15] Although these models are widely used, the static nature of the systems results in microbe overgrowth, leading to cell apoptosis within a day. Therefore, these systems cannot support co-culture systems, which are a pivotal characteristic of gut physiology.[16,17]

Over the past decade, various attempts have been made to overcome the challenges of the Transwell system through the development of dynamic microfluidic intestinal organ-on-a-chip devices. These devices mimic physiologically relevant microenvironments. For example, the HuMiX model developed by Shah et al. allowed for a long-term co-culture system with intestinal cells and complex microbial communities under anaerobic conditions.[18] Yet, this study was conducted without mechanical peristalsis, which heavily impacts microbial growth. To address this issue, Kim et al. utilized a physiologically relevant *in vitro* human "gut-on-a-chip" to stimulate gut peristalsis and fluid flow, which was also used to study intestinal inflammation.[19,20] However, a limitation of this device is that epithelial cells are exposed to continuous peristaltic flow, whereas *in vivo*, these motions are experienced periodically and not continuously. Furthermore, most gut-on-

Received: January 30, 2025
Revised: August 2, 2025
Accepted: August 4, 2025

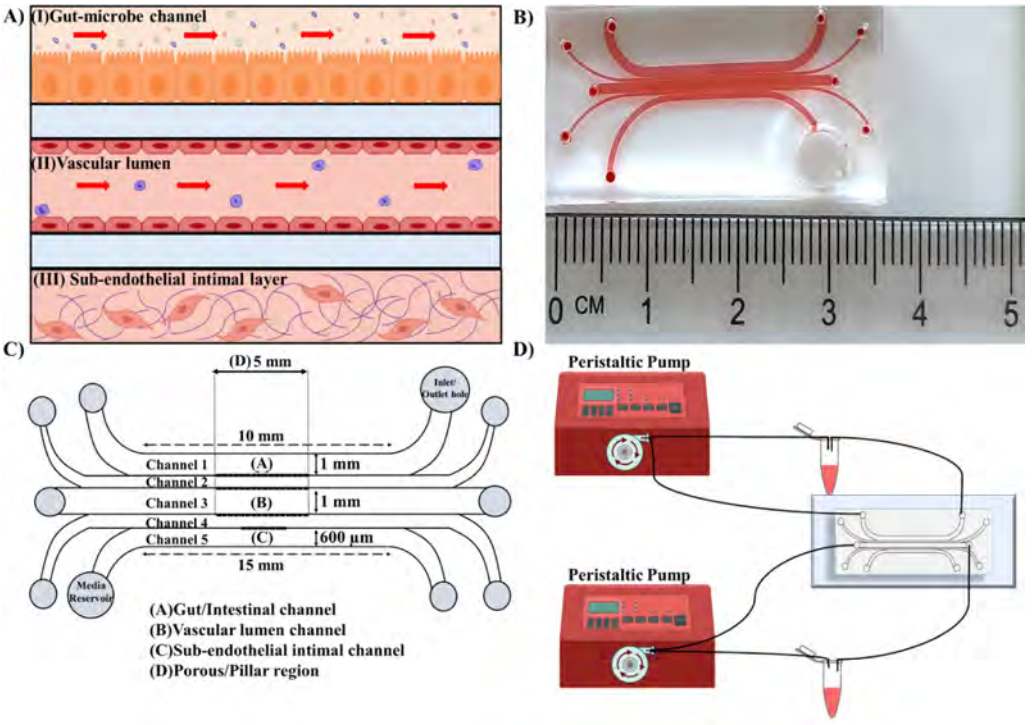

Figure 1. A multi-organ-on-a-chip model. (A) An illustration of the human gut-on-a-chip and its physiological relevance. (B) Photograph of the microfluidic multi-organ-on-a-chip model. Bright pink dye was used to highlight the separate channels, and a ruler was used to represent the relative size of the device. (C) Dimensions of the multi-organ-on-a-chip model and (D) flow setup using peristaltic pumps.

a-chip models lack supporting cells and tissue types in the intestine, including endothelial-lined blood vessels and immune cells.[21,22] These are critical for appropriate and accurate disease modeling, drug transport, and pharmacokinetic analysis.

Moreover, over the past years, there has been growing curiosity of the interaction between the human gut and inflammatory diseases, such as IBD, Rheumatoid Arthritis (RA), and possibly CVD. Previous studies have shown that lipolysaccharides (LPS) induces macrophage-derived foam cells, leading to atherosclerotic plaque formation *in vitro* and *in vivo*.[23] Additionally, a compromised gut barrier ("leaky gut") can allow microbial components to enter circulation, triggering systemic inflammation and contributing to the progression of atherosclerotic lesions. This complex gut–heart axis underscores the significance of gut health in potentially preventing and managing inflammatory diseases, such as CVDs.

Herein, we aim to develop a gut-on-a-chip model (Figure 1) for a more relevant and accurate dynamic microenvironment, as seen *in vivo*. First, we designed a novel interconnected 5-channel microfluidic device that permits a co-culture of Caco-2 cells with other supporting cells under dynamic flow conditions. We then investigated the biocompatibility of the different cells incorporated within the device. This was followed by quantitatively assessing the integrity of monolayers formed by all the cell lines using transepithelial electrical resistance (TEER), paracellular permeability assays, and membrane junction staining. This approach collectively provides an appropriate and comprehensive characterization of both epithelial and endothelial cells within the microdevice. Additionally, we assessed the effect of LPS derived from *Escherichia coli* (*E. coli*) on barrier integrity and monocyte transmigration.

2. MATERIALS AND METHODS

2.1. Microdevice Design and Fabrication. Briefly, the microfluidic chip was designed by using CleWin3 Software (WieWeb Software, The Netherlands). The master mold was fabricated in silicon using deep reactive ion dry etching, which selectively removes silicon and leaves positive features, which was done by ANFF Queensland Node. The mold was then coated with a thin layer of silane (trichloro(1*H*,1*H*,2*H*,2*H*-perfluorooctyl)(PFOCTS); Sigma-Aldrich, Cat 448931) to make the surface hydrophobic. Briefly, for salinization of the master mold, the wafer was cleaned first using pressurized nitrogen. Then, in a fume hood, two drops (using a plastic pipette) of the salinizing agent were added to an aluminum foil cap smaller than the wafer size. The foil cap, containing the salinizing agent, was covered and placed in a vacuum desiccator for 15 min (if the wafer was placed on top of the aluminum foil cap containing the silane) or 30 min (if the wafer was placed next to the aluminum foil cap containing the silane). This step made the silanes form a monolayer on the surface of the master mold. Next, the wafer was placed on a hot plate at 150 °C for 10 min to cure and evaporate the excessive silane.[24]

After that, PDMS devices were obtained using replica molding.[24−27] Briefly, liquid PDMS prepolymer was mixed with a curing agent in a standard weight ratio of 10:1 (base: curing agent) (Sylgard 184 Silicone Elastomer, Dow Corning, Midland, MI). The combined PDMS was poured over a master mold and then placed in a desiccator. The PDMS was then cured for 1 h at 75 °C. After curing, PDMS was carefully peeled from the master mold, and the inlet and outlet holes were punched with 0.75 mm biopsy punches. The PDMS slabs were carefully washed with isopropyl alcohol and water, air-dried, and kept in the oven (75 °C) for 2 min, allowing for

https://doi.org/10.1021/acsbiomaterials.5c00208
ACS Biomater. Sci. Eng. XXXX, XXX, XXX−XXX

complete drying. Next, a clean glass slide and PDMS device were treated in oxygen plasma (PDC-002, Harrick Plasma, Ossining, NY) for 1.5 min. The treated PDMS and glass slide were bonded together; this method allowed for a tight seal to be formed between the PDMS and glass slide. After bonding, the device was further cured for 10 min at 75 °C and became ready to use.[28−30]

The microfluidic device consists of five interconnected microchannels (Figure 1C). The device design was inspired by our previously developed atherothrombosis model[28] with further modifications to dimensions. The top channel mimics the gut epithelial layer and is lined with Caco-2 cells. The third and central channel represents the vascular lumen, which is lined with a murine endothelial cell line (SVEC4-10). While the bottom (fifth) channel represents the subendothelial intima, this channel is a hydrogel channel with embedded murine aortic smooth muscle cells (MOVAS). Channels two and four are hydrogel channels used to separate and act as the extracellular matrix (ECM). Each microchannel has its own inlet and outlet to allow for accurate stimulation of each channel.

The straight parts of the channels have dimensions as follows: the top channel (channel 1) has a length and width of 15 and 1 mm, respectively. Channels 2 and 4 have lengths and widths of 19 mm and 300 μm, respectively. Channel 3 has a length and width of 25 mm and 1 mm, respectively. Channel 5 has a length and width of 10 mm and 600 μm. Moreover, there are media reservoirs with a 500 μm radius and inlets and outlets punched at desirable sizes. The channels are connected via a pillar spacing structure. Briefly, to elect the relevant pillar spacing for the multiorgan-on-a-chip device, we utilized a previously designed model by Akther et al., with similar pillar spacing structures.[28,31] We investigated the diffusion of macrophages within the atherothrombosis-on-chip model, and the results suggest that 4 μm pillar spacing was appropriate as it allowed cells to migrate through the pillar spacing (Figure S1). Thus, for the multiorgan-on-a-chip device, we employed a 4 μm pillar spacing. Furthermore, the pillar structure was placed in the center of each channel covering 5 mm for channels 1−4 and 2 mm for channel 5. Finally, the height of the channels is 100 μm.

2.2. Cell Culture. The human epithelial colorectal cell line Caco-2 (ATCC, Rockville, MD) was maintained at 37 °C in a 5% CO_2 incubator in Dulbecco's Modified Eagle Medium containing 4.5 g L^{-1} glucose supplemented with 20% (v/v) fetal bovine serum (FBS) and 100 IU/mL of penicillin G, 100 μg/mL streptomycin and passaged at 80−100% confluency. Passage numbers between 20 and 65 were used. SVEC4-10 and MOVAS from ATCC, Rockville, MD, were also used. These cells were grown in low-glucose DMEM supplemented with 10% (v/v) FBS ,100 IU/mL penicillin G and 100 μg/mL streptomycin at 37 °C in a 5% CO_2 incubator. SVEC4-10 and MOVAS were used within passage numbers 3−10.

2.3. Gut and Vascular Lumen Development. The device was washed with 70% ethanol, sterile 1× PBS (pH 7.4) twice and treated under UV for 1 hr to sterilize. Then, the PDMS device was coated with hydrogel, where rat tail collagen (R&D biosystem, Cat. No. 3443-100-01) was used to form the hydrogel channels. We used collagen concentrations ranging from 2 to 4 mg/mL to determine the appropriate collagen concentration to form supporting hydrogel channels. Here, we found that 3.5 mg/mL concentration was most apt, allowing for stiffer hydrogels, reduced leakage, and decreased cell seeping into surrounding channels (Figure S2).

Briefly, to prepare 100 μL of 3.5 mg/mL collagen-neutralized hydrogel precursor solution, 10 μL of 10× low-glucose DMEM was taken into a 1.5 mL vial, and then, 70 μL of collagen stock (5 mg/mL) solution was added to the 10× DMEM. 3.5 μL of sterile NaOH (1M) was added to the solution to neutralize the collagen. Finally, deionized (DI) water was added to the solution to reach a final volume of 100 μL. A 20 μL working solution was infused through channels 2 and 4 of the devices by pipetting and incubated for 1 hr in the cell incubator (5% CO_2, 37 °C).

Then, channels 1 and 3 were coated with bovine skin collagen (Sigma-Aldrich, Cat. No. C4243). A 10 μL collagen stock (3 mg/mL) was added to 90 μL of high-glucose DMEM to get the final working concentration of 300 μg/mL. A 10-μL working solution was infused through the device and incubated for 1 h in the cell incubator (5% CO_2, 37 °C). The solution was removed, and the device was washed twice with 1× PBS. Subsequently, the device was incubated for 15 min to dry the remaining PBS.

In the meantime, Caco-2 and SVEC4-10 cells were trypsinized and detached from the flask. The cells were centrifuged at 300 × g for 5 min and resuspended in high-glucose DMEM supplemented with FBS and antibiotics. A 10-μL volume of cell suspension was infused through the channel to get the initial adhesion of Caco-2 and SVEC4-10 cells on the device wall. A suspension of Caco-2 at a concentration of 50 million/mL and a suspension of SVEC4-10 at a concentration of 30 million/mL were prepared and infused to channels 1 and 3, respectively, by careful pipetting. The density for each cell line was selected based on previous literature.[18,32,33] Approximately 10 μL of cell suspension was required to cover the whole channel. The device was placed in the cell incubator (5% CO_2, 37 °C) for 1 hr. Next, the device was placed upside down and incubated for 1 h, then followed by 1 h on each side to ensure cell attachment on all walls of the device.

2.4. Subendothelial Intimal Layer Development. In this study, to mimic the subendothelial intimal layer consisting of both vascular smooth muscle cells (VSMCs) and the ECM, we used rat tail collagen (R&D biosystem, Cat. No. 3443-100-01), a predominant ECM protein in the intima, and MOVAS.[34] Collagen concentrations ranging from 2 to 4 mg/mL with embedded MOVAS were used to determine the suitable concentration for forming an intimal layer. According to the manufacturer's protocol, to prepare 100 μL of 3 mg/mL neutralized collagen hydrogel precursor solution, 10 μL of 10× low-glucose DMEM (without FBS and antibiotics) was taken into a 1.5 mL eppendorf tube, and then 60 μL of collagen stock solution (5 mg/mL) was added, followed by adding 3 μL of sterile NaOH (1M) to neutralize the solution. A 5 μL MOVAS suspension at a concentration of 2 million/100 μL was added to the neutralized collagen solution, and the remaining volume was adjusted with deionized water. The final MOVAS concentration in the collagen solution was 100,000 cells/100 μL. 10 μL of the collagen-MOVAS suspension was perfused to channel 5 by carefully pipetting and incubating it for 1 h (5% CO_2, 37 °C) to allow for gel maturation. The device contained 10,000 MOVAS embedded in the collagen in channel 5, mimicking the subendothelial intimal layer. A reservoir was present for the subendothelial intimal layer, providing medium and supporting cell viability.

https://doi.org/10.1021/acsbiomaterials.5c00208
ACS Biomater. Sci. Eng. XXXX, XXX, XXX−XXX

2.5. Evaluation of Epithelial and Endothelial Integrity within the Microdevice. The integrity of both Caco-2 and SVEC4-10 monolayers was evaluated by membrane staining, measuring transepithelial electrical resistance (TEER), and conducting paracellular studies up to 3 days.

2.5.1. Membrane Staining. Once Caco-2 and SVEC4-10 reached confluency and covered the channels completely, the media was carefully removed and washed with PBS. Next, 4% paraformaldehyde (PFA) was added to the channels and the reservoir to fix the cells. The device was incubated for 1 h at room temperature (RT) under static conditions to allow complete fixation. The device can be stored at 4 °C or used immediately. The PFA was removed, and the channels were washed with PBS thrice. The cells were stained with CellMask™ plasma membrane stains (Invitrogen, Cat. No. C37608) for membrane staining for 20 min at RT and then washed with PBS twice before imaging. Finally, bright-field and fluorescent imaging was done using an inverted microscope (CKX53, Olympus) mounted with a digital camera (DP74, Olympus). The Z-stack images were taken using a confocal microscope (Olympus FV3000RS NIR). The images were processed and analyzed using Fiji ImageJ (Java 1.8.0_172), and the 3D image reconstruction was achieved by the Olympus FLUOVIEW (FV31S-SW) software.

2.5.2. Alcian Blue Staining. To visualize epithelial and connective tissue mucins, Alcian Blue (Sigma-Aldrich, Cat. No. 66011) stain was used. First, Caco-2 cells were rinsed with PBS and then fixed with 4% PFA for 30 min at RT. To remove the fixing agent, cells were carefully washed with PBS, and the pH was lowered using 0.1%(v/v) hydrochloric acid (HCl) for 10 min. Next, HCl was removed by rinsing with PBS, and the cells were stained with 1%(v/v) Alcian Blue stock solution for 30 min at RT. To remove excess stain, cells were rinsed at least three times with PBS. Imaging was done using the above-mentioned inverted microscope and imaging system.

2.5.3. Transepithelial Electrical Resistance (TEER) Measurements. The TEER of the Caco-2 and SVEC4-10 monolayer in the gut-on-a-chip was measured using a voltage−ohm meter (87 V Industrial Multimeter, Fluke Corporation, Everett, WA), which was coupled to Ag/AgCl electrode wires (0.008" in diameter; A-M Systems, Inc., Sequim, WA). The baseline resistance value measured in the absence of cells (R_{Blank}) was subtracted from the results obtained with the Caco-2 and SVEC4-10 monolayer (R_{Total}) (eq 1).

$$R_{TISSUE}\ (\Omega) = (R_{Total} - R_{Blank}) \tag{1}$$

The specific TEER values ($TEER_{REPORTED}$) were determined by applying eq 2. Here, we multiply the specific resistance (eq 1) by the total cell culture surface area on the PDMS membrane (the area where there is a pillar structure).[35] TEER values are typically represented ($TEER_{REPORTED}$) with a unit of Ω.cm^2 and calculated as

$$TEER_{REPORTED} = R_{TISSUE}\ (\Omega) \times M_{AREA}\ (cm^2) \tag{2}$$

where R_{TOTAL} is the resistance value of the device that contains the cells and R_{BLANK} is the blank resistance value of a microfluidic device without any cells.

2.5.4. Paracellular Permeability Measurements. For determining the permeability coefficient (P_{app}, cm s^{-1}) for the epithelial monolayer (eq 3), the transport of fluorescein isothiocyanate (FITC)-labeled dextran (FD20; 20 kDa; Sigma, St. Louis, MO) was used over a period. The Caco-2 monolayer was cultured under static or dynamic flow conditions (0.02 dyn/cm^2; ∼13.48 μL/h) for up to 3 days.[20] Subsequently, 20 μL of a working solution of 0.5 mg/mL FD20 was carefully pipetted through the top of the channel, and after 15 min, 10 μL was collected from channel 3, while simultaneously replenishing it with the same volume of fresh culture medium. Moreover, fluorescence intensity (490 nm excitation/520 nm emission) measurements of the collected samples were read to quantify the amount of FD20 transported across the Caco-2 barrier.

Similarly, the permeability coefficient of the vascular endothelial layer was determined by measuring the transport of tetramethylrhodamine isothiocyanate (TRITC)-labeled dextran (TD150; 150 kDa; Sigma, St. Louis, MO). A 20 μL working solution of 0.5 mg/mL was carefully pipetted through channel 3. After 15 min, 10 μL was collected from channel 5, while simultaneously replenishing it with the same volume of fresh culture medium. Moreover, fluorescence intensity measurements (544 nm excitation/570 nm emission) of the collected samples were read to quantify the amount of TD150 transported across the vascular lumen barrier. Before conducting the permeability experiment, the SVEC4-10 monolayer within the channel was cultured either under static or under low flow conditions 400 s^{-1} (0.04 mL/min) for 24 h and then for 48 h of incubation at an arterial shear rate of 1000 s^{-1}(0.1 mL/min).[36,37]

$$P_{app} = \frac{dQ}{dt} \times \frac{1}{A \times C_0} \tag{3}$$

where P_{app} represents the apparent permeability coefficient (cm/s), dQ/dt represents the flux of FD20 or TD150 (mg/s), the concentration is determined using a standard curve, A represents the surface area of the monolayer (cm^2), and C_0 represents the initial concentration of FD20 or TD150 perfused (mg/mL).

2.6. Microdevice Exposure to Compound. Chronic exposure to LPS in the gut can exacerbate intestinal inflammation, contribute to conditions like IBD, and disrupt gut barrier integrity, further promoting systemic inflammation. LPS is produced by bacterial surface glycolipids, which are produced by gram-negative bacteria; in the gut, LPS is produced by the following: *Enterobacter species*, *Bacteroides species*, *Escherichia coli* (*E. coli*), *Klebsiella pneumoniae*, *Clostridium species* (e.g., *Clostridium difficile*), etc.[38]

Specifically, LPS produced by Proteobacteria such as *E. coli* is often linked to intestinal disorders such as IBD and ulcerative colitis. Similarly, LPS-induced inflammation is linked to endothelial dysfunction, which impairs blood vessel function, increases arterial stiffness, and accelerates the development of atherosclerosis. To understand the impact of LPS on the integrity of epithelial cells and its effect on surrounding tissues and the vascular lumen, Caco-2 cells were exposed to LPS. Briefly, 48 h after seeding and once an intact monolayer was formed, Caco-2 cells were exposed to 50 and 200 pg/mL LPS, mimicking mild and chronic infection, respectively.[39] After 24 h, TEER measurement, paracellular studies, and membrane staining were taken to study the impact on barrier integrity, as described in Section 2.5

2.7. Preparation of Giemsa Dye. Giemsa stock solution was prepared following the previously described protocol.[39,40] To make 500 mL of Giemsa stock solution, 3.8 g of Giemsa powder (Sigma-Aldrich, G5637) was measured and poured into a clean glass bottle. Then, 100 mL of absolute methanol

https://doi.org/10.1021/acsbiomaterials.5c00208
ACS Biomater. Sci. Eng. XXXX, XXX, XXX−XXX

was added to the bottle and mixed in a circular motion for 2−3 min. Next, 250 mL of glycerol was added, and the mixture was shaken for another 3−5 min. Finally, the remaining 150 mL of absolute methanol was poured into the mixture, and the mixture was incorporated properly. The stock solution was stored in a dark and cool place, and a working solution was made by diluting the stock solution 20 times in water and used within 15 min after preparation.

2.8. Monocyte Adhesion and Transmigration in Microfluidic Device. After 24 h of treatment with LPS, we analyzed the effect of LPS on endothelial cells and the subendothelial intimal layer. We perfused channel 3 with monocytes, as seen in the case of inflammation, and monitored the adhesion and transmigration of monocytes to the subendothelial intimal layer. Monocytes (RAW 264.7 cells) were cultured in a Petri dish, tagged with Hoechst 33342 for 20 min, and washed with PBS thrice. The cells were carefully detached with a cold medium and counted using a hemocytometer. The monocyte suspension was made at 500,000 cells/mL to infuse through the channel. A syringe pump infused the monocyte suspension through the channel for 1 hr at an arterial shear rate of 1,000 s^{-1}. Images were taken at 15 min intervals to record monocyte adhesion on the SVEC-10 monolayer. The number of cells was determined using the automated particle counting option in Fiji ImageJ software. A control group without LPS stimulation was conducted to compare monocyte adhesion and subsequent transmigration to those with LPS stimulation.

After 1 h, the device was topped with fresh media and incubated under dynamic conditions with a shear rate of 1,000 s^{-1} for another 24 h to trigger subendothelial monocyte transmigration. For the quantification of monocyte transmigration in the microfluidic device, we used a previously described method.[28]

Briefly, after 24 h of incubation of monocytes under arterial shear, the surface-bound monocyte cells were detached by Trypsin by careful washing and pipetting, followed by ∼2−3 min incubation at 37 °C. Next, collagenase-D was used to liquidize and digest the subendothelial intimal layer and collect transmigrated monocytes. A 10 μL solution of 2.5 mg/mL collagenase-D in PBS was perfused through the channel and added to the media reservoir and then incubated at 37 °C for 1 hr to completely digest the collagen construct. Next, the solution was carefully extracted from the device, including the solution from the reservoir, and collected in an eppendorf tube. The device was washed three times by carefully pipetting with ∼20 μL PBS, and the washed solution was collected in the same eppendorf tube. The tube was then centrifuged at 300 × g for 5 min, the supernatant was discarded, and the cell pellet was resuspended in 10 μL of fresh media. This 10-μL suspension was pipetted on a glass slide to make a thin smear for cell counting. The slides were air-dried for 20 min at RT and blow-dried with a dryer for 10 s. Next, the slides were fixed with 78% methanol for 15 min. After this, the slides were flooded with the working solution of Giemsa (preparation procedure described in Section 2.7) and incubated for 20 min. The slides were washed with distilled water. The previously mentioned inverted microscope and imaging software were used to capture the brightfield images. Monocytes appeared with a dark purple cytoplasm in the collagen construct.

2.9. Statistical Analysis. All results were expressed as the mean ± standard deviation (SD). For statistical evaluation of quantified data, the *t*-test and one-way analysis of variance (ANOVA) with the Tukey−Kramer multiple comparisons test were performed using GraphPad version 9.5.1 (GraphPad Software Inc., San Diego, CA), where a *p-value* of ≤0.05 was considered significant.

3. RESULTS AND DISCUSSION

3.1. Gut-on-a-Chip Microsystem. In this study, we developed a microfluidic device that allows for dynamic gastrointestinal microenvironment and incorporates a vascular system. To accomplish this, our device has five interconnected microchannels: three main channels and two supporting hydrogel channels to separate the main channels, Figure 1. The top channel (channel 1) is the epithelial microchannel (referred to as the gut channel), channel 2 and 4 are the supporting hydrogel channels, and channel 3 is the vascular lumen channel. Finally, the fifth channel is the subendothelial intimal microchannel. Each channel has a porous junction region that allows the movement of microbial components (e.g., LPS and metabolites) and cells. Moreover, each channel has an inlet and outlet for sample collection, infusion, and waste removal. Furthermore, the design of this microdevice allows for real-time observation under a microscope. In addition, the system experiences dynamic fluid flow, where the gut channel experiences a flow rate of ∼13.48 μL h^{-1} to mimic the fluid flow and shear stresses of the human intestine, which have previously been shown to be ∼0.002 dyn cm^{-2}.[41−43] The vascular lumen channel experiences low flow conditions with a shear rate of 400 s^{-1}, which is then increased to 1,000 s^{-1}. The culture medium was allowed to flow through the parallel channels and experience peristaltic motion.

Caco-2 and SVEC4-10 cells bound to the collagen-coated channels after 5 h of static incubation, after which low-flow conditions (400 s^{-1}) were introduced, and confluency was achieved after 48 h of incubation at an arterial shear rate of 1,000 s^{-1}. In this microdevice, epithelial and endothelial cells grow throughout the upper and central channels, respectively, and MOVAS collagen constructs form in the lower channel.

Next, we monitored the multiorgan microdevice using a confocal microscope to confirm both epithelial and endothelial monolayers on the interconnected porous regions between the channels. Here, we took Z-stack images, Figure 2, to confirm the 3D nature and cell adhesion to the walls of the microdevice. We obtained a central angled view of the porous junction, which shows a confluent endothelial and epithelial monolayer (Figure 2A,C, respectively) across the porous region.

Similarly, a side-angled view of the vascular and gut lumen (Figure 2B,D, respectively) reveals a homogeneous and confluent monolayer across the porous junction. Moreover, using the 3D construct, we can show both the epithelium and endothelium confluently attached across the walls of the microdevice, especially along the porous region. The staining indicates the distinct wall-like barrier formed within the microdevice, mimicking that of the lumens of interest, suggesting a tight and homogeneous barrier.

3.2. Biocompatibility of Different Cells within the Microdevice. The viability of each cell line within the multiorgan-on-a-chip was established to ensure that long-term biocompatibility and prolonged co-culture systems could be sustained. Therefore, the biocompatibility of the microdevice was examined: each cell line was grown in its respective channel, and viability was measured using the LIVE/DEAD Viability/Cytotoxicity Kit over 3 days. At 24 h, Caco-2 cells

https://doi.org/10.1021/acsbiomaterials.5c00208
ACS Biomater. Sci. Eng. XXXX, XXX, XXX−XXX

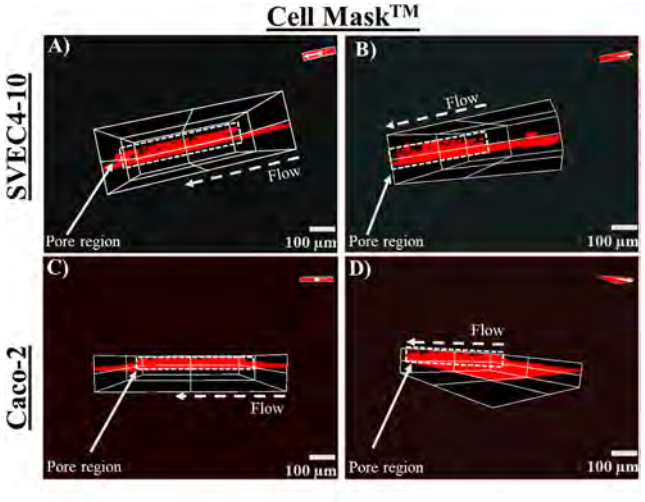

Figure 2. Confirmation of the epithelial and endothelial integrity over the porous regions between the channels is highlighted with a dashed box. (A) Front-angled and (B) side-angled views of the vascular lumen channel (channel 3) using deep red CellMask™ plasma staining and (C) front-angled and (D) side-angled views of the gut lumen (channel 1) using deep red CellMask™ membrane staining. Z-stack images were taken using a confocal microscope.

reflected above 90% viability (Figure 3D) within the microfluidic device, whereas after 48 h, viability dropped slightly but was still greater than 85% (Figure 3E), and after 72 h of incubation at 37 °C, under dynamic flow, viability still exceeded 80%, Figure 3F. The morphology of the epithelial cells after incubation within the device was also monitored, whereby they began to cluster together, forming a confluent homogeneous monolayer across the channel. Likewise, SVEC4-10 cells reflected similar results with above 80% viability after 72 h of incubation at 37 °C under dynamic flow, Figure 3J–L. We also noted that the morphology of the endothelial cells within the channel changes, whereby the SVEC4-10 cells become more elongated, Figure 3P–R, under dynamic conditions. Similarly, MOVAS cells reflected more than 95% viability within the hydrogel after 24 h of incubation, Figure 3P. After 48 h, viability remained the same, above 95%, Figure 3Q, and after 72 h of incubation at 37 °C, under dynamic flow, viability still exceeded 85%, Figure 3R.

The human intestinal epithelium is known to secrete mucus, providing a crucial protective mechanism, particularly in maintaining intestinal barrier integrity and overall gut health. Here, to verify mucus production by Caco-2 cells within the microdevice, Alcian Blue staining was conducted. Alcian Blue specifically binds to acidic mucopolysaccharides and glycoproteins, such as those found in mucin. Alcian Blue highlights the presence of secreted mucins by staining them blue, allowing us to visually confirm mucus production. Here, we see that Caco-2 cells were intensly stained (Figure 3 (**IV** and **V**)) after 48 h under dynamic conditions, suggesting mucus production.[44]

3.3. Evaluation of Barrier Intactness Under Static and Flow Conditions Using Fluorescence Staining and TEER. In this multiorgan model, we utilized Hoechst 33342 in conjunction with CellMask™ to visually confirm an intact barrier. Hoechst 33342, a blue, fluorescent dye, binds to DNA and enables the visualization of cell nuclei for accurate quantification and localization during barrier integrity assessments (Figure 4A,D). Here, CellMask™ is a lipophilic dye that specifically labels cell membranes, providing a clear delineation of cell morphology. Combined, these stains allow the simultaneous evaluation of cellular structure and integrity, facilitating the study of barrier function in assays such as tight junction analysis or permeability tests. Figure 4A,D reflects an evenly dispersed cell configuration throughout the channels for both Caco-2 and SVEC4-10, respectively. Similarly, Figure 4B,E highlights the intricate membrane network formed within the channels, allowing for tight barrier integrity. When combined (Figure 4C,F), both the internal (nuclear) and external (membrane) structures of the cells confirm an even monolayer formed across the channel. Considering barrier integrity, an intact and functional barrier is reflected by a tight, continuous arrangement of cells with well-defined borders, which can be visualized in Figure 4C,F. To further assess the functional barrier integrity, TEER and paracellular studies were carried out.

Previously, Transwell models were utilized for biological and drug studies, where Caco-2 cells were cultured on a porous Transwell membrane and tight junctional integrity was measured using TEER.[35,45,46] Unfortunately, Transwell models do not accurately represent the dynamic nature of the *in vivo* microenvironment, highlighting the importance of multiorgan models that can easily achieve these *in vivo* conditions. TEER is a non-invasive and useful technique for assessing *in vitro* barrier tissue integrity and is increasingly being used as a key metric for body-on-a-chip barrier tissue devices.[47,48]

In this study, we investigated the difference in monolayers formed under both static versus dynamic flow conditions for both Caco-2 and SVEC4-10 monolayers within our device. Results suggest that Caco-2 cells grown under flow conditions resulted in increased TEER values up to 3 days, suggesting greater barrier intactness compared to static conditions. After 24 h, Caco-2 cells grown under dynamic flow compared to static conditions reflected a 1.5-fold increase in TEER (Figure 4G). Similarly, at 48- and 72-h dynamic flow conditions, the Caco-2 monolayer reflected a 2.21- and 6.01-fold increase, respectively, in TEER compared to static conditions. This significant difference (****$p < 0.0001$) is noted between static and flow conditions after 48 and 72 h (Figure 4G). This highlights the importance of dynamic flow for an intact epithelial monolayer to be formed within the microdevice.[20,47] Epithelial barrier integrity is crucial for maintaining homeostasis in the body, as it serves as the first line of defense against environmental threats, including pathogens, toxins, and harmful substances. This barrier regulates the selective absorption of nutrients and water while preventing the entry of harmful agents into the bloodstream. When the epithelial barrier is intact, it helps maintain a balanced internal environment, supporting optimal immune function and minimizing inflammation.[49]

Similarly, TEER measurements for SVEC4-10 cells displayed a similar trend, whereby the TEER increased significantly under flow conditions compared to static conditions. Specifically, after 24 h, there was a substantial increase (****$p < 0.0001$) in TEER from static to flow conditions, reflected by a 2.02-fold increase (Figure 4H). Similarly, a significant difference (****$p < 0.0001$) was also noted between static vs flow conditions at 48 and 72 h. Here, at 48 and 72 h, dynamic flow conditions showed a 4.87- and 12.9-fold increase compared to static conditions (Figure 4H). The integrity of the endothelial barrier is vital for maintaining

https://doi.org/10.1021/acsbiomaterials.5c00208
ACS Biomater. Sci. Eng. XXXX, XXX, XXX−XXX

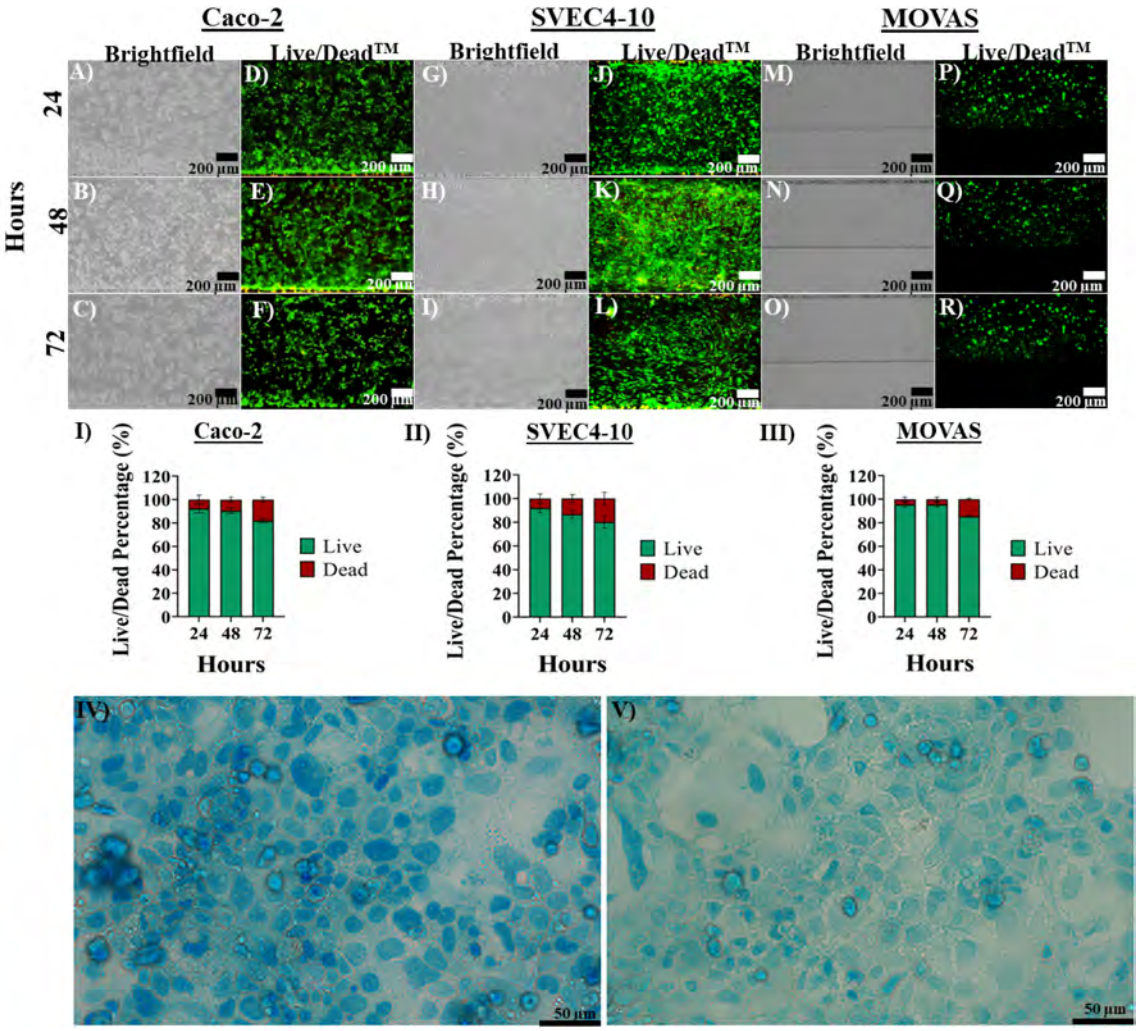

Figure 3. Caco-2, SVEC4-10, and MOVAS cell viability assays in the absence of bacteria within the microfluidic device. (A−C) Brightfield images of Caco-2 cells over 72 h. (D−F) LIVE/DEAD Viability/Cytotoxicity Kit used to assess the viability of Caco-2 cells over 72 h. (G−I) Brightfield images of SVEC4-10 cells over 72 h. (J−L) LIVE/DEAD Viability/Cytotoxicity Kit used to assess the viability of SVEC4-10 cells over 72 h. (M−O) Brightfield images of MOVAS cells over 72 h. (P−R) LIVE/DEAD Viability/Cytotoxicity Kit used to assess the viability of MOVAS cells over 72 h. (I−III) Quantitative viability of Caco-2, SVEC4-10, and MOVAS cells over 72 h using a LIVE/DEAD Viability/Cytotoxicity Kit. (IV, V) Caco-2 mucus staining with Alcian Blue, where the blue color represents mucus stained with Alcian Blue. The scale bar for images (A)−(R) is 200 μm.

homeostasis, as it regulates the movement of substances between the bloodstream and surrounding tissues. This barrier ensures proper nutrient and oxygen delivery while preventing the leakage of fluids and proteins into tissues, which could lead to edema and inflammation. A healthy endothelial barrier also plays a key role in controlling immune cell trafficking, thereby contributing to the body's defense mechanisms without triggering excessive inflammation.[50]

3.4. Paracellular Permeability Measurements Under Static and Flow Conditions. To further validate the monolayer integrity of both epithelial and endothelial cells grown within the microdevice, we also measured the paracellular permeability coefficient (P_{app}) using FD20 (Figure 4I) and TD150 (Figure 4J), respectively. This method allows for the characterization of the paracellular barrier function of both the intestinal epithelium and vascular endothelium.[51,52]

FD20 is commonly used to evaluate the paracellular barrier function of Caco-2 monolayers, which are widely used as a model for intestinal epithelial barriers.[51] By adding FD20 to the Caco-2 monolayer, we can measure its translocation to the basolateral side. The extent of FD20 permeation provides insights into the integrity of the tight junctions. The quantification of P_{app} of the intestinal epithelial barrier revealed an intact paracellular barrier function, and this monolayer displayed P_{app} values of about 3.6×10^{-8} cm s^{-1} after 3 days under flow, similar to those previously reported (Figure 4I).[53] The significant decrease in P_{app} of FD20 ($^{****}p < 0.0001$) suggests a decrease in the permeability of the compound within the Caco-2 monolayer, indicating an intact monolayer formation. Confining the movement of FD20 is key as the paracellular route allows the transportation of medium-sized hydrophilic molecules (≤600 Da *in vivo*; ≤10 kDa *in vitro* in cell lines), and normally, the paracellular route is impermeable to protein-sized molecules and thus constitutes an effective barrier to antigenic macromolecules.[54] Furthermore, the intact barrier in epithelial cells maintains low paracellular permeability, as seen by the results, by preserving the integrity of tight junctions and regulating the actin cytoskeleton. Epithelial cells under flow stimulate the expression and organization of tight junction proteins such as claudins, occludin, and zonula

https://doi.org/10.1021/acsbiomaterials.5c00208
ACS Biomater. Sci. Eng. XXXX, XXX, XXX−XXX

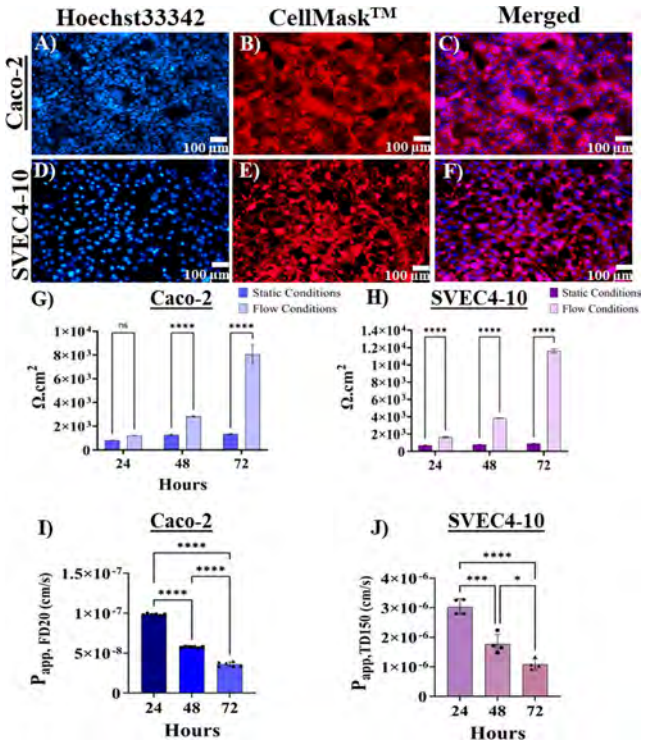

Figure 4. Reconstitution of the gut microenvironment: integrity of the Caco-2 monolayer in the microfluidic chip under both static and dynamic flow conditions. (A, D) Hoechst 33342 nuclei staining for both Caco-2 and SVEC4-10 cells, respectively. (B, E) CellMask™ membrane staining for both Caco-2 and SVEC4-10 cells, respectively. (C, F) Merged images of Caco-2 and SVEC4-10 cells, respectively, using Fiji ImageJ (Java 1.8.0_172). Images (A)−(F) were taken from the bottom surface of the microfluidic device, and the scale bar is 100 μm. (G) Caco-2 and (H) SVEC4-10 TEER study results over 72 h. (I) Caco-2 and (J) SVEC4-10 paracellular barrier study results over 72 h.

occludens 1 (ZO-1). Moreover, an upregulation of anti-inflammatory and barrier-stabilizing molecules, like AMPK and E-cadherin, has also been observed under flow in epithelial cells.[55,56]

TD150 is often used as a tracer to assess the paracellular barrier function of the vascular lumen.[36] The paracellular studies corroborate TEER results, indicating that SVEC4-10 cells could form intact homogeneous monolayers under dynamic flow conditions. Here, macromolecules above the molecular weight (MW) of albumin (>70 kDa) are retained within the lumen, while microvessels are permeable to macromolecules smaller than albumin (<70 kDa).[57] This was seen in the endothelial channel, where the movement of TD150 (150 kDa) was substantially reduced (****$p < 0.0001$) as the SVEC4-10 monolayer becomes more intact over 72 h. A 3-fold decrease in TD150 movement after 72 h was noted. Specifically, quantifying P_{app} of the intestinal endothelial barrier revealed intact paracellular barrier function, and this micro-device displayed P_{app} values of about 1.09×10^{-6} cm s^{-1} after 3 days under flow conditions (Figure 4J).[39] Moreover, flow has been shown to strengthen endothelial junctions as it upregulates junctional proteins such as VE-cadherin, claudin-5, and occludin, reinforcing tight junctions and adherens junctions. Flow conditions have also been shown to activate mechanosensors like platelet endothelial cell adhesion molecule (PECAM-1), vascular endothelial growth factor receptor 2 (VEGFR2), and integrins, triggering signaling pathways (e.g., PI3K/Akt, endothelial nitric oxide synthase (eNOS)) that promote cytoskeletal stabilization and barrier tightening.[58,59] Under physiological flow, the endothelium maintains a tight paracellular seal, limiting plasma leakage and immune cell extravasation.[60,61]

3.5. Effect of LPS Derived from *E. coli In Vitro*. In the gut, LPS is typically contained within the intestinal lumen, but disruptions in the gut barrier, such as those caused by dysbiosis, inflammation, or injury, allow LPS to translocate into the bloodstream. Once in circulation, LPS acts as a powerful immune activator, triggering systemic inflammatory responses through the activation of Toll-like receptor 4 (TLR4) in immune cells.

LPS was perfused through the gut channel to mimic infectious conditions, and its impact on both the gut and vascular channels was assessed. Quantitative data suggested a substantial reduction in epithelial and endothelial barrier integrity after being treated with LPS under mild and chronic infection conditions, 50 pg mL^{-1} and 200 pg mL^{-1}, respectively.

Specifically, the microfluidic device was exposed to LPS after 72 h. When treated with mild infection conditions, Caco-2 cells reflected a reduction (***$p < 0.001$) in TEER, compared to the 96-h control group, which reflected a continued increase in TEER (Figure 5H). Under chronic infection conditions, we saw a significant decrease (****$p < 0.0001$) in TEER (Figure 5H) after 24 h of treatment. Similarly, SVEC4-10 cells, after being treated with mild and chronic infection conditions, both reflected a substantial reduction (****$p < 0.0001$) in integrity according to TEER readings (Figure 5J). For both cell lines, the results demonstrated that LPS-treated monolayers, under both mild and chronic conditions, led to a breached monolayer, as reflected by the significant reduction in TEER.

To better understand the effect of LPS on the barrier, a paracellular permeability assay was performed. Caco-2 and SVEC4-10 monolayers cultured in the microdevice were further assessed by studying the behavior of FD20 and TD150, respectively. Here, we observed that the permeability of FD20 was significantly increased (****$p < 0.0001$) after incubation with both concentrations of LPS (Figure 5G), suggesting significant impairment to epithelial barrier integrity. Increased permeability of FD20 indicates a compromised barrier function, suggesting that LPS affects barrier integrity, which is a common characteristic of gut dysbiosis and inflammatory diseases such as IBD.[62,63]

After the gut lumen was treated with LPS, we monitored its effect on the vascular channel. Although not directly treated, the vascular channel was also substantially damaged, ****$p < 0.0001$ (Figure 5I). An increase in TD150 permeability typically indicates compromised barrier function, which may be associated with various pathological conditions, such as inflammation or vascular diseases.[23] This characterization is crucial for understanding endothelial health and the underlying mechanisms that contribute to vascular permeability in both normal physiology and disease states. There has been no multiorgan-on-a-chip device that has been able to show impairment mirroring this effect.

The results demonstrated that adding LPS permeabilized the Caco-2 and SVEC4-10 monolayers and allowed the substantial transport of FD20 and TD150, respectively. In Caco-2 cells, LPS exposure led to increased paracellular permeability, as evidenced by alterations in TEER and the increased flux of

https://doi.org/10.1021/acsbiomaterials.5c00208
ACS Biomater. Sci. Eng. XXXX, XXX, XXX−XXX

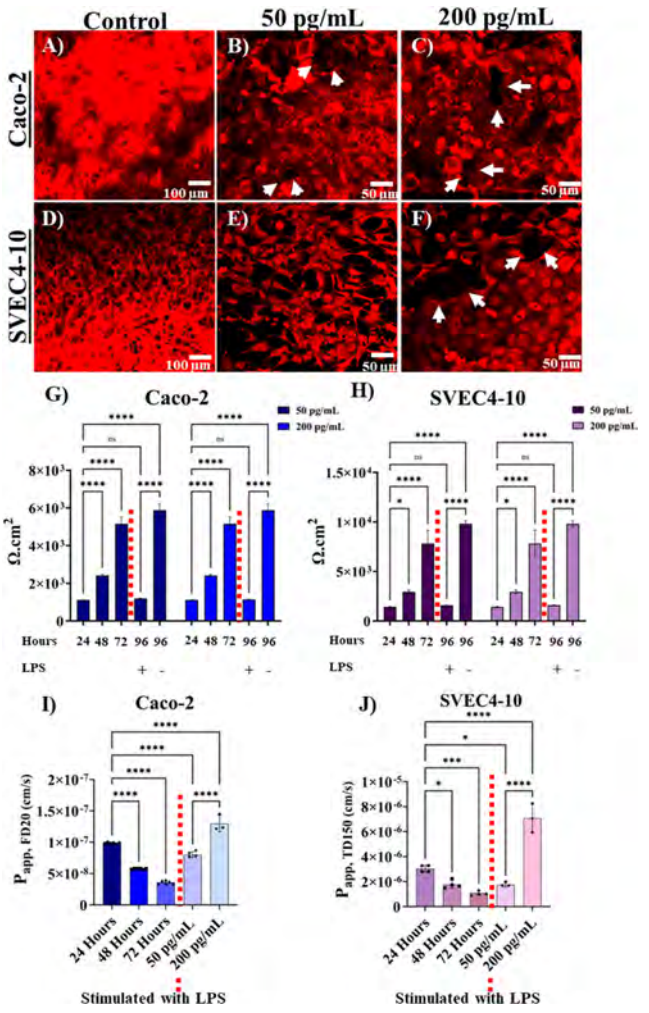

Figure 5. Effect of LPS derived from *E. coli* on the gut and consequently the vascular microenvironment. The barrier integrity of both endothelial and epithelial monolayers in a microfluidic chip under dynamic flow conditions was determined using cell membrane staining, TEER, and dextran. CellMask™ membrane staining for (A) SVEC4-10 control group (without LPS treatment), (B) mild (50 pg/mL), and (C) chronic (200 pg/mL) LPS treatment of SVEC4-10. (D) Caco-2 control group (without LPS treatment), (E) mild (50 pg/mL), and (F) chronic (200 pg/mL) LPS treatment of Caco-2 cells. Evident deterioration in the Caco-2 and SVEC-10 monolayers with junction leakiness was seen and marked by white arrows. The TEER study on (G) Caco-2 and (H) SVEC4-10 before and after LPS treatment. Paracellular barrier studies on (I) Caco-2-10 and (J) SVEC4-10 before and after LPS treatment.

FD20. This disruption facilitates the translocation of pathogens and toxins from the gut lumen into the systemic circulation, prompting a cascade of immune responses. Similarly, in SVEC4-10 cells, LPS exposure enhanced permeability by modulating endothelial barrier function, contributing to increased vascular leakage.[63]

Ultimately, the interaction between LPS and these monolayers underscores the importance of inflammatory mediators in altering permeability and highlights potential mechanisms underlying intestinal and vascular pathologies associated with bacterial infections, gut dysbiosis, etc. This altered microbiome composition, favoring pathogenic over beneficial bacteria, may consequently lead to dysbiosis, which can exacerbate inflammation, perpetuating a vicious cycle that further compromises gut barrier function and systemic health.[62,64,65]

3.6. LPS Derived from *E. coli* Affects Monocyte Adhesion and Transmigration. A hallmark in systemic inflammation but also early atherosclerosis is the migration of monocytes to the subendothelial layer of the intima, where they may differentiate into macrophages or dendritic cells.[66−69] In this study, we observed monocyte adhesion and transmigration as seen *in vivo* under inflammatory conditions. First, we treated the gut channel with LPS with mild and chronic infection conditions, as mentioned previously. Under mild infection conditions, we saw some monocyte adhesion to the endothelial monolayer after 1 h under arterial shear flow, an ∼7.1-fold increase compared to the control group (no LPS stimulation). Moreover, compared to the non-stimulated group, we saw some significance, $p < 0.05$, after 1 h. We also saw a gradual increase in monocyte adhesion to the vascular lumen channel over time (Figure 6A). Next, we observed the potential for monocyte transmigration into the subendothelial intima. Surprisingly, after the mild infection treatment, there was no significant difference compared to the control when studying the transmigration of monocytes to the subendothelial intima (Figure 6B). Giemsa staining also suggests no significant difference from the control conditions (Figure 6D).

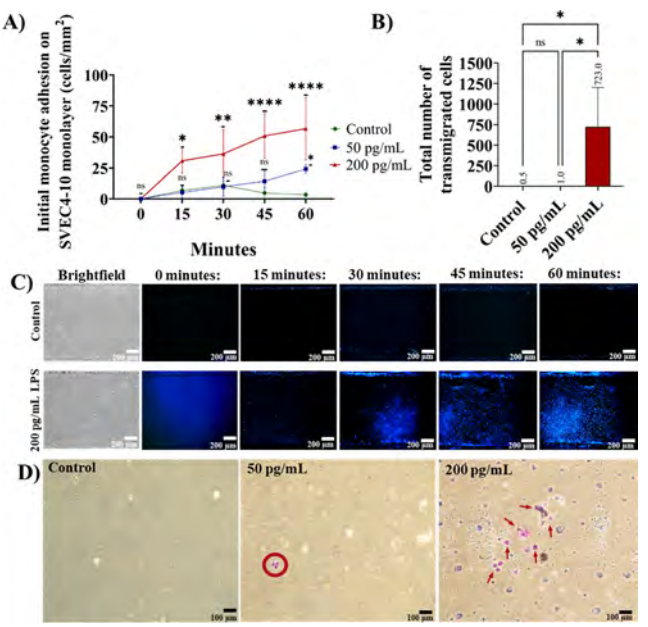

Figure 6. Monocyte transmigration and Giemsa staining in a microfluidic multiorgan-on-a-chip model. (A) Initial monocyte adhesion on the SVEC4-10 monolayer mimicking the vascular lumen, spanning an area of 1.64 mm². The gut lumen channel was treated with LPS (50 and 200 pg/mL) prior to monocyte infusion, and the control group was not treated. (B) The total number of transmigrated cells into the subendothelial intimal layer (bottom channel) after 24 h incubation under an arterial shear rate. (C) Fluorescence images of the initial adherent monocytes on the SVEC4-10 monolayer in the control group and the LPS (200 pg/mL) stimulated group at different time points. The blue color (Hoechst 33342) indicated adherent monocytes. (D) Microscopic images of Giemsa stained with the thin smear of the transmigrated cells in the control group, 50 pg/mL and 200 pg/mL LPS-stimulated groups. The monocytes gave a strong purple/pink color with an apparently smooth rounded morphology (red arrow). Values are mean ± SD, $n = 5$, *t*-test. $^{*}p < 0.05$, $^{**}p < 0.01$, and $^{****}p < 0.0001$.

https://doi.org/10.1021/acsbiomaterials.5c00208
ACS Biomater. Sci. Eng. XXXX, XXX, XXX−XXX

However, when treated with chronic infection conditions, we observed a significant increase in monocyte adhesion after 1 h of perfusion and at each time point compared to the control (Figure 6A). Notably, after 1 h under arterial shear flow, we observed that monocyte adhesion increased 2.3-fold, compared to mild infectious conditions, and showed a 16.6-fold increase compared to the control. With chronic infection (200 pg/mL^{-1} LPS), we noted a significant increase (****$p < 0.0001$) to ∼723 monocytes found in the subendothelial intimal layer (Figure 6B). This is due to a notably impaired barrier in both Caco-2 and endothelial monolayers after treatment of LPS as also seen in TEER results in Figure 5H,J. From the Giemsa staining, we can observe that monocytes have a rounded morphology with a noticeable purple color (Figure 6D), as noted in previous studies.[70,71] Here, the chronic infection group displayed significantly larger monocyte transmigration than the mild infection group and the control.

Individuals with chronic inflammatory conditions often exhibit a gut microbial profile that is more pro-inflammatory compared to healthy individuals.[72,73] A compromised epithelial or endothelial barrier is instrumental in promoting immune cell infiltration during the early stages of inflammation by altering surface markers and releasing inflammatory mediators.[74] In typical situations, the endothelium serves as a blockade, stopping circulating monocytes from adhering (Figure 6C, control).

However, in response to triggers like oxidative stress, microbial dysbiosis, or systemic inflammation, epithelial and endothelial cells express adhesion molecules such as ICAM-1 and VCAM-1, facilitating monocyte attachment (Figure 6C (LPS-stimulated)). Moreover, the dysfunctional endothelium also releases pro-inflammatory cytokines, which increase the attraction and movement of monocytes into the subendothelial area, as seen in our model by the significantly increased monocyte adhesion in our LPS-treated groups vs control (Figure 6B). After arriving, monocytes can transform into macrophages, enhancing inflammatory reactions.[75] This procedure highlights the important role of endothelial dysfunction in initiating atherosclerosis. This mechanism underscores the central role of barrier dysfunction and immune cell recruitment in the pathogenesis of various inflammatory diseases. More importantly, this multiorgan model could mimic the mechanism of possible early inflammation often seen in IBD, atherosclerosis progression, etc.

4. CONCLUSION AND FUTURE PERSPECTIVES

In this study, we developed a 3D gut-on-a-chip model, which can be used to study and further understand the gut−heart interactions and its impact on inflammatory diseases, including possibly the development of early atherosclerosis. This model could sustain biocompatibility of over 80% viability of all cell lines utilized over 3 days. Furthermore, a homogeneous monolayer was established within the microdevice confirmed using TEER, paracellular permeability assays, and membrane staining. Next, we induced a state of infection caused by LPS, resulting in an evident destabilization of barrier integrity, often seen in the state of dysbiosis and chronic inflammation. Moreover, this microfluidic platform could mimic *in vivo*-like monocyte transmigration often seen in inflammatory diseases, such as IBD, RA, and atherosclerosis. Additionally, this model was able to recreate a physiologically relevant microenvironment, including all appropriate *in vivo* components, such as a vascular layer and a subintimal layer. Our model can be useful for studying the risk of gut microbiota in the development of inflammatory diseases, such as IBD and atherosclerosis. This model can also be used as a platform for drug testing by targeting patient-specific mechanisms.

However, further optimization of this model is required to allow for prolonged microbial incorporation. Some limitations of this proof-of-concept study are the lack of investigation of the secretion of key inflammatory chemokines and cytokines, as well as the expression of adhesion molecules (e.g., VCAM). Some other key cellular mechanisms that can be investigated include smooth muscle cell proliferation and phenotypic alterations of VSMCs. Phenotypic alterations include assessing specific markers, such as contractile and synthetic markers. Specifically, α-smooth muscle actin (α-SMA), smooth muscle myosin heavy chain (SM-MHC), and calponin indicate a contractile phenotype. For synthetic markers, osteopontin, matrix metalloproteinases (MMPs), and growth factors (e.g., platelet-derived growth factor, PDGF) reflect a synthetic migratory phenotype. In the future, we can utilize patient-derived cells to recreate patient-specific microenvironments and expand the use of this model for patient-specific therapeutic development.

■ ASSOCIATED CONTENT

Data Availability Statement

Data are available upon request from the authors.

Supporting Information

The Supporting Information is available free of charge at https://pubs.acs.org/doi/10.1021/acsbiomaterials.5c00208.

Perfusion flow rate determination, pillar spacing determination (Figure S1), and optimization of rat tail collagen hydrogel (Figure S2) (PDF)

■ AUTHOR INFORMATION

Corresponding Author

Hang Thu Ta − *School of Environment and Science, Griffith University, Nathan, Queensland 4111, Australia; Queensland Quantum and Advanced Technologies Research Institute, Griffith University, Nathan, Queensland 4111, Australia;* orcid.org/0000-0003-1188-0472; Phone: +61 (7) 3735 5384; Email: h.ta@griffith.edu.au

Authors

Dimple Sajin − *School of Environment and Science, Griffith University, Nathan, Queensland 4111, Australia; Queensland Quantum and Advanced Technologies Research Institute, Griffith University, Nathan, Queensland 4111, Australia*

Shehzahdi S. Moonshi − *Queensland Quantum and Advanced Technologies Research Institute, Griffith University, Nathan, Queensland 4111, Australia;* orcid.org/0000-0003-2048-595X

Haotian Cha − *Queensland Quantum and Advanced Technologies Research Institute, Griffith University, Nathan, Queensland 4111, Australia*

Fahima Akther − *Australian Institute for Nanotechnology and Bioengineering, University of Queensland, St Lucia 4072, Australia*

Jun Zhang − *Queensland Quantum and Advanced Technologies Research Institute, Griffith University, Nathan, Queensland 4111, Australia; School of Engineering and Built Environment, Griffith University, Nathan QLD 4111, Australia;* orcid.org/0000-0003-1113-6264

Nam-Trung Nguyen − *Queensland Quantum and Advanced Technologies Research Institute, Griffith University, Nathan, Queensland 4111, Australia; School of Engineering and Built Environment, Griffith University, Nathan QLD 4111, Australia;* orcid.org/0000-0003-3626-5361

Complete contact information is available at: https://pubs.acs.org/10.1021/acsbiomaterials.5c00208

Notes

The authors declare no competing financial interest.

■ ACKNOWLEDGMENTS

This work is funded by the National Health and Medical Research Council (HTT: APP1182347, APP2002827) and the Heart Foundation (HTT: 102761). The authors would like to acknowledge the Australian National Fabrication Facility (Queensland Node) for access to key items of equipment. Hang Thu Ta is supported by an ARC Future Fellowship (FT240100280) and a Heart Foundation Future Leader Fellowship (102761). Dimple Sajin's PhD scholarship is provided by Hang Thu Ta funding (102761) and Griffith University.

■ ABBREVIATIONS

α-SMA	A-smooth muscle actin
CRP	C-reactive protein
CVD	Cardiovascular disease
DI	Deionized
DMEM	Dulbecco's Modified Eagle Medium
ECM	Extracellular matrix
E. coli	*Escherichia coli*
eNOS	Endothelial nitric oxide synthase
FBS	Fetal bovine serum
FITC	Fluorescein isothiocyanate
HCl	Hydrochloric acid
IBD	Inflammatory bowel disease
LPS	Lipopolysaccharides
MMPs	Matrix metalloproteinases
MOVAS	Murine aortic smooth muscle cells
P_{app}	Paracellular permeability coefficient
PDGF	Platelet-derived growth factor
PECAM-1	Platelet endothelial cell adhesion molecule
PFA	Paraformaldehyde
PFOCTS	Trichloro(1*H*,1*H*,2*H*,2*H*-perfluorooctyl) silane
RA	Rheumatoid arthritis
RT	Room temperature
SD	Standard deviation
SM-MHC	Smooth muscle myosin heavy chain
TEER	Transepithelial electrical resistance
TLR4	Toll-like receptor 4
TRITC	Tetramethylrhodamine isothiocyanate
VEGFR2	Vascular endothelial growth factor receptor 2
VSMCs	Vascular smooth muscle cells
ZO-1	Zonula occludens-1

■ REFERENCES

(1) de Vos, W. M.; Tilg, H.; Van Hul, M.; Cani, P. D; et al. Gut microbiome and health: mechanistic insights. *Gut* **2022**, *71* (5), 1020−1032.

(2) Garrett, W. S.; Gordon, J. I.; Glimcher, L. H. Homeostasis and inflammation in the intestine. *Cell* **2010**, *140* (6), 859−870.

(3) Regnier, M.; et al. Gut microbiome, endocrine control of gut barrier function and metabolic diseases. *J. Endocrinol* **2021**, *248* (2), R67−R82.

(4) Parker, B. J.; Wearsch, P. A.; Veloo, A. C. M.; Rodriguez-Palacios, A. The Genus Alistipes: Gut Bacteria With Emerging Implications to Inflammation, Cancer, and Mental Health. *Front. Immunol* **2020**, *11*, 906.

(5) Ahmad, A. F.; et al. The gut microbiome and cardiovascular disease: current knowledge and clinical potential. *Am. J. Physiol. Heart Circ. Physiol* **2019**, *317* (5), H923−H938.

(6) Pant, A.; et al. Human Gut Microbiota and Drug Metabolism. *Microb. Ecol* **2023**, *86* (1), 97−111.

(7) Weersma, R. K.; Zhernakova, A.; Fu, J. Interaction between drugs and the gut microbiome. *Gut* **2020**, *69* (8), 1510−1519.

(8) Tang, W. H. W.; Li, D. Y.; Hazen, S. L. Dietary metabolism, the gut microbiome, and heart failure. *Nat. Rev. Cardiol* **2019**, *16* (3), 137−154.

(9) Puschhof, J.; et al. Intestinal organoid cocultures with microbes. *Nat. Protoc* **2021**, *16* (10), 4633−4649.

(10) Grosheva, I.; et al. High-Throughput Screen Identifies Host and Microbiota Regulators of Intestinal Barrier Function. *Gastroenterology* **2020**, *159* (5), 1807−1823.

(11) Trapecar, M.; Communal, C.; Velazquez, J.; Maass, C. A.; Huang, Y.-J.; Schneider, K.; Wright, C. W.; Butty, V.; Eng, G.; Yilmaz, O.; et al. Gut-Liver Physiomimetics Reveal Paradoxical Modulation of IBD-Related Inflammation by Short-Chain Fatty Acids. *Cell Syst* **2020**, *10* (3), 223−239.e9.

(12) Calatayud, M.; et al. Development of a host-microbiome model of the small intestine. *FASEB J* **2019**, *33* (3), 3985−3996.

(13) Vizoso Pinto, M. G.; et al. Lactobacilli stimulate the innate immune response and modulate the TLR expression of HT29 intestinal epithelial cells in vitro. *Int. J. Food Microbiol* **2009**, *133* (1−2), 86−93.

(14) Shin, W.; Kim, H. J. 3D in vitro morphogenesis of human intestinal epithelium in a gut-on-a-chip or a hybrid chip with a cell culture insert. *Nat. Protoc* **2022**, *17* (3), 910−939.

(15) Lee, Y.; Kim, S. J.; Park, J.-K. Chips-on-a-plate device for monitoring cellular migration in a microchannel-based intestinal follicle-associated epithelium model. *Biomicrofluidics* **2019**, *13* (6), 064127.

(16) Bruck, W. M.; Graverholt, G.; Gibson, G. R. A two-stage continuous culture system to study the effect of supplemental alpha-lactalbumin and glycomacropeptide on mixed cultures of human gut bacteria challenged with enteropathogenic *Escherichia coli* and *Salmonella* serotype Typhimurium. *J. Appl. Microbiol* **2003**, *95* (1), 44−53.

(17) Macfarlane, S.; et al. Polysaccharide degradation by human intestinal bacteria during growth under multi-substrate limiting conditions in a three-stage continuous culture system. *FEMS Microbiol. Ecol* **1998**, *26* (3), 231−243.

(18) Shah, P.; Fritz, J. V.; Glaab, E.; Desai, M. S.; Greenhalgh, K.; Frachet, A.; Niegowska, M.; Estes, M.; Jäger, C.; Seguin-Devaux, C.; et al. A microfluidics-based in vitro model of the gastrointestinal human−microbe interface. *Nat. Commun* **2016**, *7*, 11535.

(19) Kim, H. J.; Li, H.; Collins, J. J.; Ingber, D. E.; et al. Contributions of microbiome and mechanical deformation to intestinal bacterial overgrowth and inflammation in a human gut-on-a-chip. *Proc. Natl. Acad. Sci. U. S. A* **2016**, *113* (1), No. E7−E15.

(20) Kim, H. J.; et al. Human gut-on-a-chip inhabited by microbial flora that experiences intestinal peristalsis-like motions and flow. *Lab Chip* **2012**, *12* (12), 2165−2174.

(21) Maynard, C. L.; et al. Reciprocal interactions of the intestinal microbiota and immune system. *Nature* **2012**, *489* (7415), 231−241.

(22) Mahler, G. J.; et al. Characterization of a gastrointestinal tract microscale cell culture analog used to predict drug toxicity. *Biotechnol. Bioeng* **2009**, *104* (1), 193−205.

(23) Yuan, H.; et al. LPS-induced autophagy is mediated by oxidative signaling in cardiomyocytes and is associated with

cytoprotection. *Am. J. Physiol. Heart Circ. Physiol* **2009**, *296* (2), H470−9.
(24) Lin, C.; Khetani, S. R. Micropatterned Co-Cultures of Human Hepatocytes and Stromal Cells for the Assessment of Drug Clearance and Drug-Drug Interactions. *Curr. Protoc. Toxicol* **2017**, *72*, 14.17.1−14.17.23.
(25) Zhang, J.; et al. High-Throughput Separation of White Blood Cells From Whole Blood Using Inertial Microfluidics. *IEEE Trans. Biomed. Circuits Syst* **2017**, *11* (6), 1422−1430.
(26) Zhang, J.; et al. Inertial Microfluidic Purification of Floating Cancer Cells for Drug Screening and Three-Dimensional Tumor Models. *Anal. Chem* **2020**, *92* (17), 11558−11564.
(27) Whitesides, G. M.; et al. Soft lithography in biology and biochemistry. *Annu. Rev. Biomed. Eng* **2001**, *3*, 335−373.
(28) Akther, F.; Zhang, J.; Tran, H. D. N.; Fallahi, H.; Adelnia, H.; Phan, H.-P.; Nguyen, N.-T.; Ta, H. T. Atherothrombosis-on-Chip: A Site-Specific Microfluidic Model for Thrombus Formation and Drug Discovery. *Adv. Biol* **2022**, *6* (7), No. e2101316.
(29) Thomas, D. P.; Zhang, J.; Nguyen, N.-T.; Ta, H. T.; et al. Microfluidic Gut-on-a-Chip: Fundamentals and Challenges. *Biosensors* **2023**, *13* (1), 136.
(30) Fallahi, H.; et al. On-demand deterministic release of particles and cells using stretchable microfluidics. *Nanoscale Horiz* **2022**, *7* (4), 414−424.
(31) Akther, F.; Fallahi, H.; Zhang, J.; Nguyen, N.-T.; Ta, H. T.; et al. Evaluating thrombosis risk and patient-specific treatment strategy using an atherothrombosis-on-chip model. Lab on a Chip. *Lab Chip* **2024**, *24* (11), 2927−2943.
(32) Sontheimer-Phelps, A.; et al. Human Colon-on-a-Chip Enables Continuous In Vitro Analysis of Colon Mucus Layer Accumulation and Physiology. *Cell Mo.L Gastroenterol Hepatol* **2020**, *9* (3), 507−526.
(33) Akther, F.; et al. An intimal-lumen model in a microfluidic device: potential platform for atherosclerosis-related studies. *Lab Chip* **2025**, *25* (3), 354−369.
(34) Akther, F.; et al. Hydrogels as artificial matrices for cell seeding in microfluidic devices. *RSC Adv* **2020**, *10* (71), 43682−43703.
(35) Srinivasan, B.; et al. TEER measurement techniques for in vitro barrier model systems. *J. Lab. Autom* **2015**, *20* (2), 107−126.
(36) van Duinen, V.; van den Heuvel, A.; Trietsch, S. J.; Lanz, H. L.; van Gils, J. M.; van Zonneveld, A. J.; Vulto, P.; Hankemeier, T. 96 perfusable blood vessels to study vascular permeability in vitro. *Sci. Rep* **2017**, *7* (1), 18071.
(37) Ungell, A.-L.; Artursson, P. An Overview of Caco-2 and Alternatives for Prediction of Intestinal Drug Transport and Absorption. *Drug Bioavailability* **2008**, *40*, 133−159.
(38) d'Hennezel, E.; Abubucker, S.; Murphy, L. O.; Cullen, T. W.; et al. Total Lipopolysaccharide from the Human Gut Microbiome Silences Toll-Like Receptor Signaling. *mSystems* **2017**, *7* (1), 18071.
(39) Akther, F.; Sajin, D.; Moonshi, S. S.; Wu, Y.; Vazquez-Prada, K. X.; Ta, H. T. Modeling Foam Cell Formation in A Hydrogel-Based 3D-Intimal Model: A Study of The Role of Multi-Diseases During Early Atherosclerosis. *Adv. Biol* **2024**, *8* (4), No. e2300463.
(40) Jaworowski, A.; Hearps, A. C.; Angelovich, T. A.; Hoy, J. F.; et al. How Monocytes Contribute to Increased Risk of Atherosclerosis in Virologically-Suppressed HIV-Positive Individuals Receiving Combination Antiretroviral Therapy. *Front. Immunol* **2019**, *10*, 1378.
(41) Gijzen, L.; et al. An Intestine-on-a-Chip Model of Plug-and-Play Modularity to Study Inflammatory Processes. *SLAS Technol* **2020**, *25* (6), 585−597.
(42) Lentle, R. G.; Janssen, P. W. Physical characteristics of digesta and their influence on flow and mixing in the mammalian intestine: a review. *J Comp Physiol B* **2008**, *178* (6), 673−690.
(43) Ishikawa, T.; et al. Transport phenomena of microbial flora in the small intestine with peristalsis. *J. Theor. Biol* **2011**, *279* (1), 63−73.
(44) Ude, V. C.; Brown, D. M.; Stone, V.; Johnston, H. J. Using 3D gastrointestinal tract in vitro models with microfold cells and mucus secreting ability to assess the hazard of copper oxide nanomaterials. *J. Nanobiotechnol* **2019**, *17* (1), 70.
(45) Sun, T.; et al. On-chip epithelial barrier function assays using electrical impedance spectroscopy. *Lab Chip* **2010**, *10* (12), 1611−1617.
(46) Li, B. R.; Wu, J.; Li, H.-S.; Jiang, Z.-H.; Zhou, X. M.; Xu, C.-H.; Ding, N.; Zha, J.-M.; He, W.-Q.; et al. In Vitro and In Vivo Approaches to Determine Intestinal Epithelial Cell Permeability. *J. Vis. Exp* **2018**, *19* (140), 57032.
(47) Tan, H. Y.; et al. A multi-chamber microfluidic intestinal barrier model using Caco-2 cells for drug transport studies. *PLoS One* **2018**, *13* (5), No. e0197101.
(48) Malik, M.; Steele, S. A.; Mitra, D.; Long, C. J.; Hickman, J. J. Trans-epithelial/endothelial electrical resistance (TEER): Current state of integrated TEER measurements in organ-on-a-chip devices. *Curr. Opin. Biomed. Eng* **2025**, *34*, 100588.
(49) Ghosh, S. S.; et al. Intestinal Barrier Dysfunction, LPS Translocation, and Disease Development. *J. Endocr Soc* **2020**, *4* (2), bvz039.
(50) Yuan, S. Y.; Rigor, R. R. *Regulation of Endothelial Barrier Function*; San Rafael: California, 2010.
(51) Schoultz, I.; Keita, Å. V. The Intestinal Barrier and Current Techniques for the Assessment of Gut Permeability. *Cells* **2020**, *9* (8), 1909.
(52) Elbrecht, D.; Long, C. J.; Hickman, J. J. Transepithelial/endothelial Electrical Resistance (TEER) theory and applications for microfluidic body-on-a-chip devices; *J. Rare Dis. Res. Treat.*, **2016**; *1*.
(53) Jalili-Firoozinezhad, S.; et al. A complex human gut microbiome cultured in an anaerobic intestine-on-a-chip. *Nat. Biomed. Eng* **2019**, *3* (7), 520−531.
(54) Martin-Padura, I.; et al. Junctional adhesion molecule, a novel member of the immunoglobulin superfamily that distributes at intercellular junctions and modulates monocyte transmigration. *J. Cell Biol* **1998**, *142* (1), 117−127.
(55) Tang, V. W.; Goodenough, D. A. Paracellular ion channel at the tight junction. *Biophys. J* **2003**, *84* (3), 1660−1673.
(56) Buddington, R. K.; Wong, T.; Howard, S. C. Paracellular Filtration Secretion Driven by Mechanical Force Contributes to Small Intestinal Fluid Dynamics. *Med. Sci* **2021**, *9* (1), 9.
(57) Mundi, S.; et al. Endothelial permeability, LDL deposition, and cardiovascular risk factors-a review. *Cardiovasc. Res* **2018**, *114* (1), 35−52.
(58) Cheng, H.; et al. Effects of shear stress on vascular endothelial functions in atherosclerosis and potential therapeutic approaches. *Biomed. Pharmacother* **2023**, *158*, 114198.
(59) Conway, D. E.; Schwartz, M. A. Mechanotransduction of shear stress occurs through changes in VE-cadherin and PECAM-1 tension: implications for cell migration. *Cell Adh Migr* **2015**, *9* (5), 335−339.
(60) Tarbell, J. M. Shear stress and the endothelial transport barrier. *Cardiovasc. Res* **2010**, *87* (2), 320−330.
(61) Baratchi, S.; Knoerzer, M.; Khoshmanesh, K.; Mitchell, A.; McIntyre, P. Shear Stress Regulates TRPV4 Channel Clustering and Translocation from Adherens Junctions to the Basal Membrane. *Sci. Rep* **2017**, *7* (1), 15942.
(62) Guo, S.; et al. Lipopolysaccharide causes an increase in intestinal tight junction permeability in vitro and in vivo by inducing enterocyte membrane expression and localization of TLR-4 and CD14. *Am. J. Pathol* **2013**, *182* (2), 375−387.
(63) Stephens, M.; von der Weid, P. Y. Lipopolysaccharides modulate intestinal epithelial permeability and inflammation in a species-specific manner. *Gut Microbes* **2020**, *11* (3), 421−432.
(64) Candelli, M.; Franza, L.; Pignataro, G.; Ojetti, V.; Covino, M.; Piccioni, A.; Gasbarrini, A.; Franceschi, F. Interaction between Lipopolysaccharide and Gut Microbiota in Inflammatory Bowel Diseases. *Int. J. Mol. Sci* **2021**, *22* (12), 6242.
(65) An, L.; et al. The Role of Gut-Derived Lipopolysaccharides and the Intestinal Barrier in Fatty Liver Diseases. *J. Gastrointest. Surg* **2022**, *26* (3), 671−683.

https://doi.org/10.1021/acsbiomaterials.5c00208
ACS Biomater. Sci. Eng. XXXX, XXX, XXX−XXX

(66) Bobryshev, Y. V. Monocyte recruitment and foam cell formation in atherosclerosis. *Micron* **2006**, *37* (3), 208−222.
(67) Pickett, J. R.; et al. Targeting endothelial vascular cell adhesion molecule-1 in atherosclerosis: drug discovery and development of vascular cell adhesion molecule-1−directed novel therapeutics. *Cardiovasc. Res* **2023**, *119* (13), 2278−2293.
(68) Pickett, J. R.; Wu, Y.; Ta, H. T. VCAM-1 as a common biomarker in inflammatory bowel disease and colorectal cancer: unveiling the dual anti-inflammatory and anti-cancer capacities of anti-VCAM-1 therapies. *Cancer Metastasis Rev* **2025**, *44* (2), 40.
(69) Perera, B.; et al. Advances in drug delivery to atherosclerosis: Investigating the efficiency of different nanomaterials employed for different type of drugs. *Mater. Today Bio* **2023**, *22*, 100767.
(70) Angelovich, T. A.; et al. Ex vivo foam cell formation is enhanced in monocytes from older individuals by both extrinsic and intrinsic mechanisms. *Exp. Gerontol* **2016**, *80*, 17−26.
(71) Angelovich, T. A.; Hearps, A. C.; Maisa, A.; Kelesidis, T.; Jaworowski, A.; et al. Quantification of Monocyte Transmigration and Foam Cell Formation from Individuals with Chronic Inflammatory Conditions. *J. Vis. Exp* **2017**, *2017* (128), 56293.
(72) Jie, Z.; Xia, H.; Zhong, S.-L.; Feng, Q.; Li, S.; Liang, S.; Zhong, H.; Liu, Z.; Gao, Y.; Zhao, H.; et al. The gut microbiome in atherosclerotic cardiovascular disease. *Nat. Commun* **2017**, *8* (1), 845.
(73) Emoto, T.; et al. Analysis of Gut Microbiota in Coronary Artery Disease Patients: a Possible Link between Gut Microbiota and Coronary Artery Disease. *J. Atheroscler Thromb* **2016**, *23* (8), 908−921.
(74) Woollard, K. J.; Geissmann, F. Monocytes in atherosclerosis: subsets and functions. *Nat. Rev. Cardiol* **2010**, *7* (2), 77−86.
(75) Cretoiu, D.; Ionescu, R. F.; Enache, R. M.; Cretoiu, S. M.; Voinea, S. C.; et al. Gut Microbiome, Functional Food, Atherosclerosis, and Vascular Calcifications—Is There a Missing Link? *Microorganisms* **2021**, *9* (9), 1913.

https://doi.org/10.1021/acsbiomaterials.5c00208
ACS Biomater. Sci. Eng. XXXX, XXX, XXX−XXX

Supplementary data for

Multi-organ-on-a-chip: The gut and inflammatory diseases

Dimple Sajin [1,2], Shehzahdi S. Moonshi[2], Haotian Cha[2], Fahima Akther[3], Jun Zhang[2,4], Nam-Trung Nguyen[2,4], Hang Thu Ta[1,2,3,*]

[1]School of Environment and Science, Griffith University, Nathan, Queensland, 4111, Australia

[2]Queensland Quantum and Advanced Technologies Research Institute, Griffith University, Nathan, Queensland, 4111, Australia

[3]Australian Institute for Nanotechnology and Bioengineering, University of Queensland, St Lucia 4072, Australia

[4]School of Engineering and Built Environment, Griffith University, Nathan, QLD 4111, Australia

*Correspondence: Hang Thu Ta (h.ta@griffith.edu.au)

1. Perfusion flow rate

To convert the arterial shear rate (1,000 s^{-1}) into flow rate, we used Newton's law of viscosity. Briefly, Newton's law of viscosity:

$\tau = \eta \times \frac{dv}{dx}$

Where, τ = shear stress, η = viscosity (Pa.s) and $\frac{dv}{dx}$ = shear rate (s^{-1})

dyn/cm^2 is often used as dynamic viscosity unit instead of Pa.s in the cardiovascular system.

As 1 Pa = 10 $dyn.s/cm^2$, The dynamic viscosity of media= 8.9×10^{-3} $dyn.s/cm^2$

** Here, we use the dynamic viscosity of water as dynamic viscosity of media.

To convert 1000 s^{-1} at flow rate, we calculated as,

$\tau = 8.9 \times 10^{-3}$ $dyn.s/cm^2 \times 1000$ s^{-1}

$= 8.9$ dyn/cm^2 (1)

The shear stress was calculated using the following equation,

$\tau = \frac{6\eta Q}{h2w}$ (2)

Here, τ: shear stress; h: height of the channel= 100 μm= 0.010 cm; w: width of the channel= 1 mm= 0.1 cm; η: dynamic viscosity of the media ($dyn.s/cm^2$) = 8.9×10^{-3} $dyn.s/cm^2$; Q: Flow rate

By rearranging equation 2 and taking the value from equation 1,

$Q = \tau(h^2 w)/6\eta$

$= 8.9$ $dyn.s/cm^2$ $(0.010^2$ cm^2 x 0.1 cm)/(6 ×(8.9 x 10^{-3}) $(dyn.s)/cm^2$))

= 1.67 x 10^{-3} cm^3 /s

We know, 1 cm^3 = 1 ml,

Q = 1.67 x 10^{-3} cm^3 /s = 1.67 x 10^{-3} mL/s = (1.67 x 10^{-3} mL/s) x 60 mL/min

= 0.1 mL/min = 100 µl/min or 6mL/hr (~ 1000 s^{-1})

Similarly, to calculate flow rate for gut lumen channel, we used the same equation as above, where to mimic fluid flow and shear stresses of the human intestine, which have previously been shown to be ~0.002–0.08 dyne cm^{-2}.

In this study, we chose 0.02 dyn.s/cm^2, by exposing our gut microchannel to dynamic flow of 13.48 µL/hr.

$Q = \tau(h^2 w)/6\eta$

= 0.02 dyn.s/cm^2 (0.010^2 cm^2 x 0.1 cm)/(6 ×(8.9 x 10^{-3}) (dyn.s)/cm^2))

= 3.745^{-3} x $10^{-6}$$cm^3$ /s

We know, 1 cm^3 = 1 ml,

Q = 3.745^{-3} x 10^{-6} cm^3 /s = 3.745^{-3} x 10^{-6} mL/s

= (3.745^{-3} x 10^{-6} mL/s) x 60 mL/min

= 2.247 x 10^{-4} mL/min x 60 mL/hr

= 0.013 mL/hr or 13.48 uL/hr

2. Pillar spacing determination

To determine the relevant pillar spacing for the multi-organ-on-a-chip device we utilised a previously designed model by Akther, F., et al., with similar features containing pillar spacing

structure. [1] Briefly, RAW 264.7 cells were cultured in a Petri dish, tagged with Hoechst 33342 for 20 min and washed with PBS thrice. The cells were carefully detached with a cold medium and counted using a hemocytometer. The monocyte suspension was made at 500,000 cells/mL to infuse through the channel. A syringe pump infused the monocyte suspension through the channel for an hour at the arterial shear rate of 1,000 s^{-1}. [1] Images were taken at 15-minute intervals to record monocytes movement across the channels through the porous region (region where there is pillar structure).

We conducted preliminary experiments to investigate the diffusion rate of macrophages over different time intervals within an atherothrombosis-on-chip model previously designed by our team. [1] This analysis provided an idea of the parameters and optimal pillar spacings for our multi-organ device. The dimension of the atherothrombosis-on-chip model is as follows, the width of the main channel and the supporting channel are 200 and 100 µm, respectively. Both channels are interconnected by a 400 µm long porous region. The height of both channels is 50 µm. Following the protocol described above, RAW264.7 macrophages were stained and perfused into the top channel, whereby diffusion into the supporting hydrogel channel was monitored at 0, 2, 4, 6, and 24 hours. Here, we tested a device with a pillar spacing of 4 µm, as we hypothesised pillar spacing of greater than 8 µm is too large, allowing cells to diffuse without stimulation.

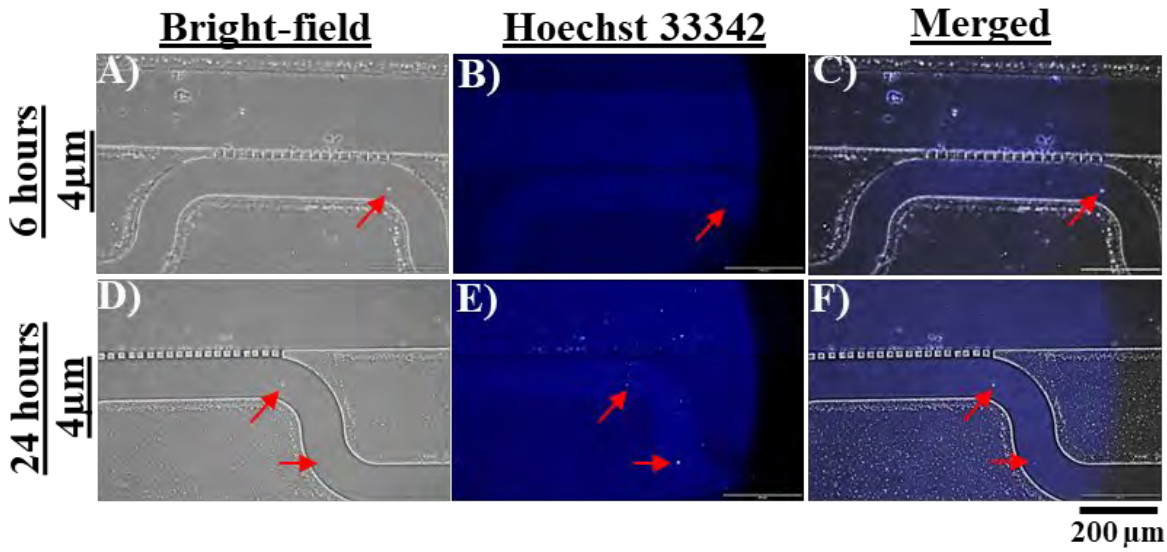

Figure S1: Macrophages unstimulated diffusion experiment of a microfluidic device with 4 µm pillar spacings. **A)** Bright-field image with focus on hydrogel region of microfluidic chip with 4 µm pillar spacings after 6 hours; **B)** Fluorescent image with focus on hydrogel region of microfluidic chip with 4 µm pillar spacings after 6 hours; **C)** Merged image of with a focus on hydrogel region of microfluidic chip with 4 µm pillar spacings after 6 hours; **D)** Bright-field image of microfluidic chip with 4 µm pillar spacings after 24 hours; **E)** Fluorescent image of microfluidic chip with 4 µm pillar spacings after 24 hours; **F)** Merged image of microfluidic chip with 4 µm pillar spacings after 24 hours. The scalebar for all images is 200 µm.

Results from these unstimulated macrophage diffusion studies suggest that devices with the 4 µm pillar spacing allowed for cells to slowly diffuse into the supporting hydrogel channel. Theoretically, RAW264.7 macrophages typically have a size range of 10-20 microns in diameter. Since macrophages are motile cells, they are capable of migrating through the ECM to sites of inflammation. Changes within the mechanical microenvironment such as stiffness, hydrodynamics, and pH, all impact the migration and diffusion of these cells. [2] A slow progression of the macrophages is noted, believed to be due to the absence of a stimulant (e.g., interferon-γ (IFN- γ) or LPS) to draw them to the hydrogel. In the presence of such a stimulant, it is hypothesised that migration will be quicker and more directional. Since the multi-organ-

on-a-chip has pillars separating each cell line, the size of each cell line had to be considered before finalising pillar spacings. Epithelial cells typically have a diameter from 8 to 21 microns; enterocytes are about 8-10 µm wide with a height of 25 µm. [3] Furthermore, endothelial cells vary in size depending on their distribution across the vascular tree, generally they are 50- 70 µm long, 10-30 µm wide and 0.1-10 µm thickness. [4] The Caco-2 cells, used in the multi-organ-on-a-chip, are a cell model of the small intestine with an enterocyte-like phenotype, similarly, SVEC4-10 is an endothelial cell line. Thus, Caco-2 and SVEC4-10 cells have similar morphology and phenotypes to epithelial and endothelial cells respectively, including size. Taken together pillar spacing of 4 µm is appropriate as it allowed for cell migration through the pillar spacing, so this pillar spacing was employed for the multi-organ-on-a-chip.

Table S1: Different concentrations of Rat tail Collagen hydrogel composition for optimisation for the multi-organ-on-a-chip model.

Final Concentration	Rat tail Collagen (Stock 5 mg/mL)	DMEM (10X)	NaOH	Deionised (DI) Water or Cell suspension
2 mg/mL	40 µL	10 µL	2 µL	48 µL
2.5 mg/mL	50 µL	10 µL	2.5 µL	37.5 µL
3 mg/mL	60 µL	10 µL	3 µL	27 µL
3.5 mg/mL	70 µL	10 µL	3.5 µL	16.5 µL
4 mg/mL	80 µL	10 µL	4 µL	6 µL

3. **Optimisation of hydrogel concentrations**

Previously, our atherothrombosis-on-chip model [5] utilised hydrogel concentration of 2 mg/mL, but translating it to the multi-organ-on-a-chip model resulted in leakage of cells between channels. This led to the optimisation of hydrogel concentrations.

Table S1, were prepared and incorporated into the multi-organ-on-a-chip model for optimisation (**Figure S2**). To determine the optimal hydrogel concentrations for the

microdevice, we tested various concentrations ranging from 2.5 mg/mL to 4 mg/mL (**Table S1**). Briefly, to prepare 100 µL of 3 mg/mL collagen-neutralized hydrogel precursor solution, 10 µL of 10 × low glucose DMEM was taken into a 1.5 mL vial, and then 60 µL of collagen stock (5 mg/mL) solution was added to the 10X DMEM. 3 µL sterile NaOH (1M) was added to the solution to neutralize the collagen. Finally, deionized (DI) water was added to the solution to reach a volume of up to 100 µL. A 10 µL working solution was infused through the device and incubated for an hour in the cell incubator (5% CO_2, 37°C).

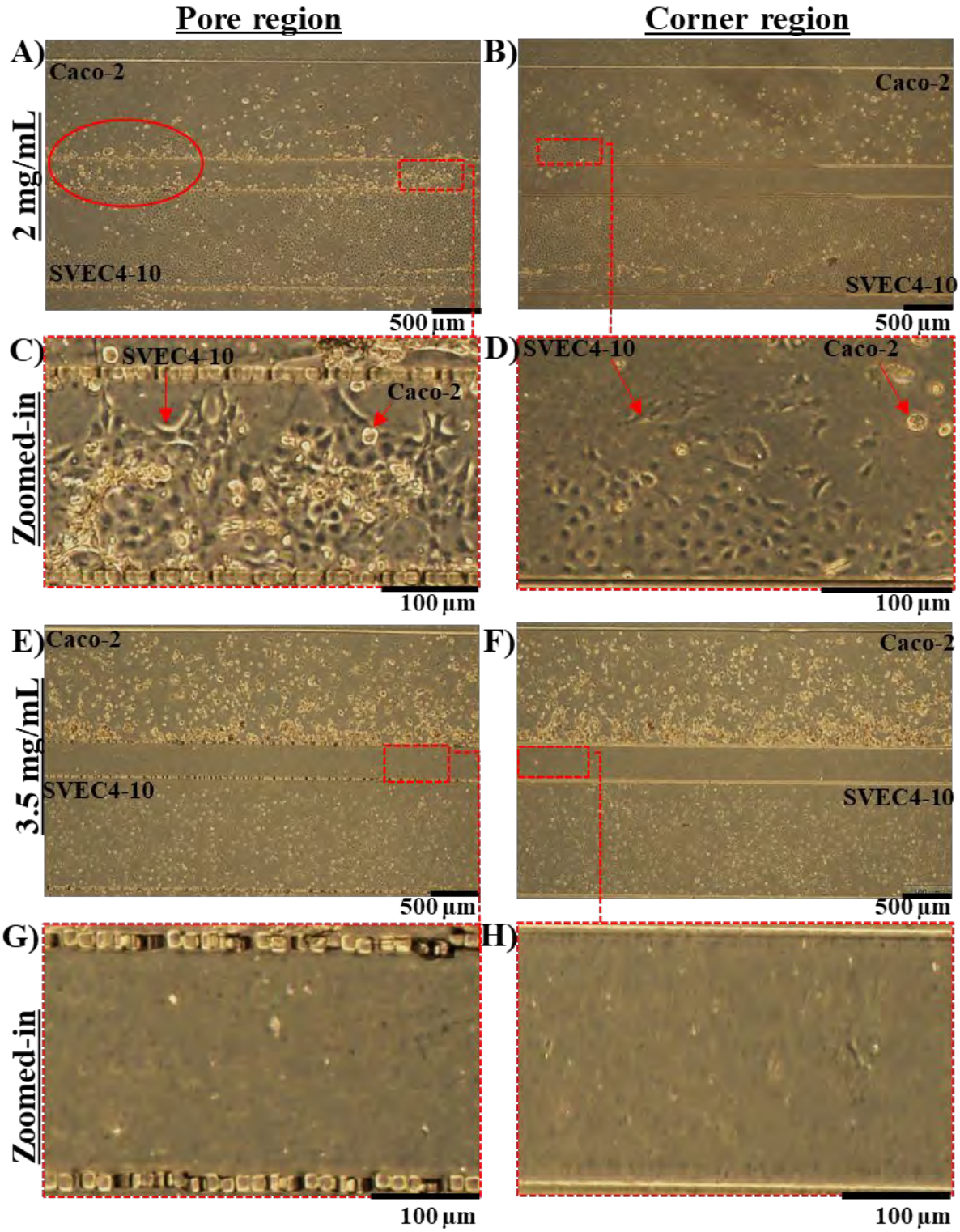

Figure S2: Optimisation of hydrogel concentration on multi-organ-on-a-chip model. **A)** The 4 µm pore region of model with 2 mg/mL of hydrogel after 24 hours; **B)** The corner regions of model with 2 mg/mL of hydrogel after 24 hours; **C)** Zoomed-in image of the leakage with SVEC4-10 cells in hydrogel region; **D)** Zoomed-in image of the leakage with SVEC4-10 cells

in gut channel containing Caco-2 cells; **E)** The 4 µm pore region of model with 3.5 mg/mL of hydrogel after 24 hours; **F)** The corner regions of model with 3.5 mg/mL of hydrogel after 24 hours.; **G)** Zoomed-in image of Caco-2 cells to show density and distribution in multi-organ-on-a-chip with 3.5 mg/mL of hydrogel; **H)** Zoomed-in image of SVEC4-10 cells to show density and distribution in multi-organ-on-a-chip with 3.5 mg/mL of hydrogel. Images C, D, G and H are cropped and zoomed images.

Concentrations of 2 and 3.5 mg/mL were utilised in the multi-organ-on-a-chip model, whereby the lower concentration of collagen (2 mg/mL) (**Figure S2A &B**) resulted in undesirable movement of cells into both the porous and corner regions of the supporting hydrogel channels. We observed SVEC4-10 cells seep into the hydrogel channel, Channel 2, (**Figure S2C**) separating the gut and vascular lumen channels. In the corner regions of the channel, we see SVEC4-10 cells permeating inside the gut channel with the Caco-2 cells (**Figure S2D**). These cells were distinguished and determined based on their morphology. Moreover, 2.5 and 3 mg/mL concentrations of collagen also reflected slight leakage. Whereas 3.5 mg/mL (**Figure S2E - H**) of collagen produced the stiffer hydrogel resulting in reduced movement of the cells (**Figure S2 E & F**) to porous and corner regions of the supporting hydrogel channels. 4 mg/mL was also tested, the hydrogel formed was too stiff and dried out too quickly. It was concluded that 3.5 mg/mL is the most apt hydrogel concentration, allowing for a stiff hydrogel, reduced leakage, and cell seepage into surrounding channels (**Figure S2G & H**).

References:

1. Akther, F., et al., *Atherothrombosis-on-Chip: A Site-Specific Microfluidic Model for Thrombus Formation and Drug Discovery.* Adv Biol (Weinh), 2022. **6**(7): p. e2101316.
2. Perez-Rodriguez, S., et al., *A microfluidic-based analysis of 3D macrophage migration after stimulation by Mycobacterium, Salmonella and Escherichia.* BMC Microbiol, 2022. **22**(1): p. 211.
3. Brown, N.A. and A.J. Bron, *An estimate of the human lens epithelial cell size in vivo.* Exp Eye Res, 1987. **44**(6): p. 899-906.
4. Pham, T.T., et al., *Quantitative characterization of endothelial cell morphologies depending on shear stress in different blood vessels of domestic pigs using a focused ion beam and high resolution scanning electron microscopy (FIB-SEM).* Tissue Cell, 2015. **47**(2): p. 205-12.

5. Akther, F., et al., *Modeling Foam Cell Formation in A Hydrogel-Based 3D-Intimal Model: A Study of The Role of Multi-Diseases During Early Atherosclerosis.* Adv Biol (Weinh), 2024. **8**(4): p. e2300463.